European Journal of Clinical Pharmacy
Print ISSN: 2385-409X **Online ISSN**: 3105-0409
Website: https://farmclin.es/

$MnNiBa_2O_4$ Nanoparticles for Enhanced Photocatalytic Degradation of a Group of Dye

Article History:

Name of Author:
Jinesh Menaria[1], Dushyant Kumar Prajapati[2], Jeevan Kunwar Chouhan[3], Tejveer Singh Tanwer[4], Shipra Bhardwaj[5]

Affiliation:
[1,2,3,4]Research scholars, [5]Professor
Department of Chemistry, Government Meera Girls College, Mohan Lal Shukhadia University, Udaipur, Rajasthan, India -313001

Corresponding Author:
Jinesh Menaria
Mail id: menariajinesh1992@gmail.com

Received:02-01-2026
Accepted: 20-01-2026
Published: 06-02-2026

Abstract:
$MnNiBa_2O_4$ nanoparticles were synthesized via co-precipitation method and systematically characterized using XRD, FE-SEM/EDX, PL, UV-Vis, and XPS across different calcination temperatures. These nanoparticles exhibited a direct optical band gap of 3.25 eV with strong absorbance at 464 nm, confirming visible-light photocatalytic potential. **Objectives:** Develop and optimize quaternary $MnNiBa_2O_4$ nanoparticles for efficient photocatalytic degradation of textile dye—toluidine blue (TB),. **Methods:** Co-precipitation synthesis with calcination optimization; comprehensive characterization; Tauc plot analysis; reactive species scavenging experiments; four-cycle reusability assessment. **Findings:** Achieved 81-85% dye degradation within 60 minutes; photogenerated holes (h^+) identified as primary reactive specie; maintained consistent photocatalytic performance over four successive cycles. **Novelty:** Mn-Ni-Ba-O quaternary oxide system demonstrating superior visible-light-driven textile dye degradation with calcination temperature optimization and confirmed reactive specie mechanism, offering promising wastewater treatment solution.

Keywords: Photocatalysis, Photodegradation, Coprecipitation, Dye Degradation, Water treatment.

INTRODUCTION

Industrial textile dyes severely contaminate aquatic ecosystems, presenting significant toxicity risks to aquatic life and human health due to their chemical stability, persistence, and carcinogenic properties. These synthetic colorants, including azo and triarylmethane dyes, resist natural biodegradation and block light penetration essential for photosynthesis in water bodies. Photocatalysis emerges as a green, sustainable remediation strategy, employing semiconductor materials that absorb light to generate electron-hole pairs, producing reactive oxygen species (ROS) like hydroxy radicals and super oxide radical to mineralize dyes into CO_2, H_2O, and innocuous by-products [1][2]. Mn oxides such as MnO_2 and Mn_3O_4 stand out for their versatile oxidation states (Mn^{3+}/Mn^{4+} redox couples), which enable efficient charge separation and transfer while maintaining narrow bandgaps (typically 1.5–3 eV) responsive to visible light. These properties drive high ROS generation, achieving over 90% degradation of recalcitrant dyes like methylene blue and malachite green, often enhanced by their large surface area and strong pollutant adsorption [3-5]. NiO nanoparticles contribute p-type semiconducting behaviour with a wide bandgap (~3.6 eV) and abundant oxygen vacancies that promote visible-light harvesting and hydroxy radical formation through suppressed electron-hole recombination. Studies report 90–96% degradation efficiencies for dyes under UV or solar irradiation, attributed to NiO's catalytic sites and stability in aqueous media [6][7]. BaO enhances dye uptake via its basic surface sites, provides structural stabilization in composites, and modulates bandgaps (4–5 eV range), fostering efficient heterojunctions that accelerate charge migration [8][9]. The synthesized $MnNiBa_2O_4$ nanoparticles synergistically combine Mn's redox versatility, Ni's electrical conductivity, and Ba's robust framework, yielding an optimized 3.25 eV bandgap ideal for visible-light

photocatalysis, enabling 81–85% dye removal in 60 min with reusability.

METHODOLOGY

Materials and method

$MnCl_2{\cdot}4H_2O$ (5 g, Merck), $NiCl_2{\cdot}6H_2O$ (11.88 g, Merck), and $Ba(NO_3)_2$ (13.06 g, Merck) were used as precursors for synthesis of $MnNiBa_2O_4$ by coprecipitation method. sodium hydroxide pellets (NaOH, 96%, Merck Co. Ltd.), HCl (BDH), toluidine blue (TB), reactive red-35 (RR), and eosin yellow (EY), EDTA, ether, isopropyl alcohol, sulphuric acid, hydrochloric acid, etc. of different make were used of high quality and analytical grade with 99% purity. Double distilled water was used all over the work. For kinetic study, dye solutions were placed in beakers, photocatalyst was added and exposed to a 200Watt tungsten lamp. The light intensity was measured by solarimeter (New CHEM Dt 1307). Optical density (OD) of solutions was recorded at different time intervals on a spectrophotometer (CHINO). pH of the solutions was measured by pH meter (Hena pen type). A linear plot of log (OD) versus time confirmed pseudo-first-order degradation kinetics (Figure 8).

Instrumentation

A Panalytical X Pert Pro X-ray diffractometer with Ni-filtered Cu Kα radiation (40 kV, 40 mA) and monochromatized Cu Kα (λ = 1.5418 Å) scanned 4-80° (2θ). Nova Nano FE-SEM 450 (FEI) scanning electron microscopy examined surface roughness and morphology with energy-dispersive X-ray compositional analysis. Physical Electronics instruments provided XPS spectra (Model: PHI 5000 VersaProbe III). A Perkin Elmer UV-vis NIR spectrophotometer measured UV-vis diffuse reflectance spectra. PL data was analysed by a perkin-elmer fl 8500 fl85k21010402 200323

The absorbance of the dye was measured using a UV–Vis spectrophotometer (CHINO). Using the following formula, the degradation percentage of the dyes was calculated:

% degradation = Ao – At/ Ao × 100

Where, Ao and At represent the initial absorbance and final absorbance of the dye at different time intervals, respectively.

RESULT AND DISCUSSION

Synthesis:

$MnNiBa_2O_4$ quaternary nanocomposite photocatalyst was prepared via straightforward co-precipitation method. 0.1 M solutions of $MnCl_2{\cdot}4H_2O$ (5 g, pH 5.9), $NiCl_2{\cdot}6H_2O$ (11.88 g, pH 5.6), and Ba $(NO_3)_2$ (13.06 g, pH 7.2) were prepared. The solution was then filtered, combined, and stirred for 2 hours at 25°C to yield transparent solution (pH 5.2). Dropwise 5N NaOH addition under stirring precipitated solid (final pH 9.5), followed by 30-min settling. The solution was then filtered, washed and dried at 120°C. pulverization, and 500°C/4h calcination produced 26.12 g brownish-black semiconductor, the yield % was 90.72.

Characterization via diverse analytical methods and degradation mechanism is reported here by:

EDX analytical study:

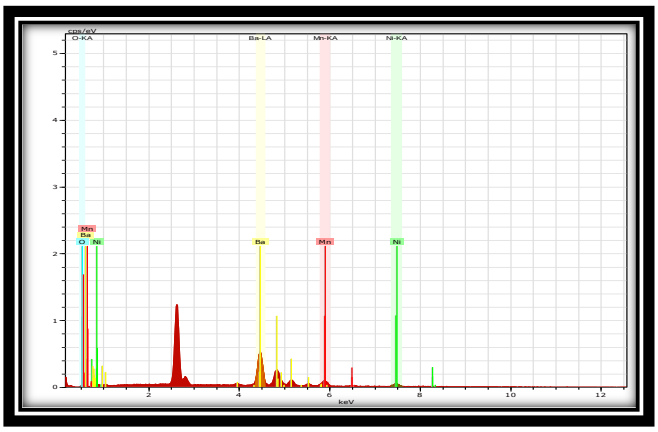

Figure 1. EDX Spectra with elemental mapping of $MnNiBa_2O_4$ nanoparticle

Table 1. Elemental Composition of $MnNiBa_2O_4$ Photocatalyst

Element	Weight%	Atomic%
Ba L	59.88	24.22
Mn K	11.67	11.8
Ni K	13.78	13.04
O K	14.67	50.94
Totals	100.00	

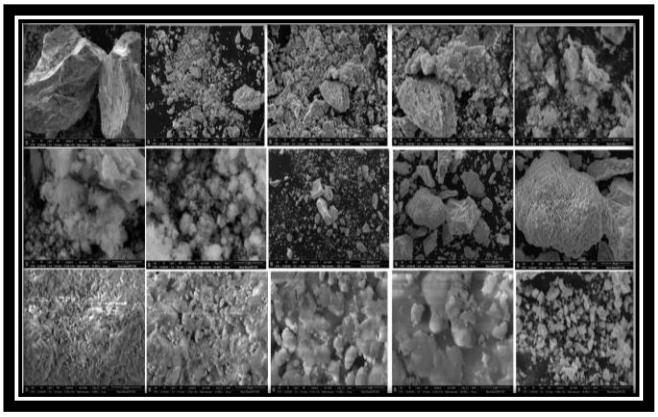

Figure 2. FESEM images of $MnNiBa_2O_4$ photocatalyst

EDX analysis of $MnNiBa_2O_4$ nanoparticles (Figure 1, Table 1) verifies stoichiometry with Mn:Ni:Ba:O weight ratios of 1:1:2:4, confirming successful quaternary synthesis. FESEM images (Figure 2) display highly agglomerated powder comprising micron-scale flakes/granules from nanosized

primaries, validating compositional integrity and catalytic-ready surface morphology.

XPS analytical study:

XPS analysis elucidates the electronic structure and oxidation states within $MnNiBa_2O_4$ mixed oxide components. High-resolution spectra (Figure 3) reveal Ba 3d doublet (Ba $3d_5/_2$ at 779.7 eV, Ba $3d_3/_2$ at 795.0 eV) indicative of Ba^{2+} in oxides [10][11]; Mn $2p_3/_2$ main peak (641 eV) with 651 eV satellite confirms Mn^{2+} in Mn-O bonds [12- 14]; Ni $2p_3/_2$ at 854 eV verifies Ni^{2+} in NiO structures establishing +2 states dominance in this photocatalyst [14][15].

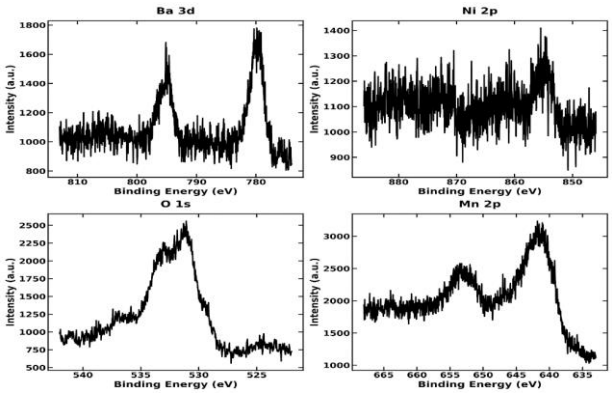

Figure 3. XPS spectra of individual elements

Crystal size calculation:

Powder X-ray diffraction (XRD) analysis confirmed the high crystallinity and phase purity of synthesized $MnNiBa_2O_4$ nanoparticles (Figure 4, Table 2). The diffraction pattern exhibits sharp Bragg reflections, with the most intense peak at $2\theta \approx 32.02°$ corresponding to the (110) plane (d-spacing = 2.79 Å, 100% relative intensity), indicating preferred crystal growth orientation [16].

Significant peaks at 2θ = 24.19° (100), 26.44° (101), 29.62° (102), 37.33° (200), 41.92° (201), 43.42° (004), 45.79° (202), and 56.74° (211) match a hexagonal perovskite-related structure similar to $BaMnO_3$ (JCPDS 26-0168), verifying formation of a single-phase mixed Mn-Ni-Ba oxide without impurity peaks (MnO, NiO, BaO)[16][17].

Debye-Scherrer analysis of the dominant peak (FWHM ≈ 0.2285°) yielded ~36.2 nm crystallite size (33–36 nm average), characteristic of nanostructured photocatalysts with enhanced surface area for superior dye degradation performance [18-20].

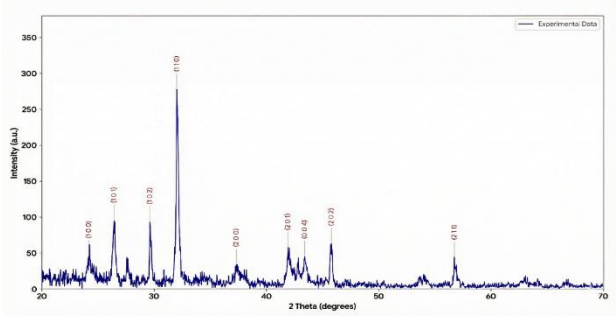

Figure 4. XRD pattern of $MnNiBa_2O_4$ photocatalyst

Table 2. Crystal size of $MnNiBa_2O_4$ photocatalyst

S. No.	Angle 2θ	d-spacing (Å)	FWHM	Relative Intensity (%)	Crystal size (nm)	Average crystal size (nm)
1.	24.19	3.6770	0.0535	16.5	151.97	
2.	24.25	3.6680	0.1283	22.2	63.34	
3.	26.44	3.3689	0.2949	34.3	27.68	
4.	26.50	3.3614	0.0239	33.5	341.06	
5.	27.58	3.2322	0.1032	15.8	79.25	
6.	27.67	3.2219	0.0385	15.1	212.61	
7.	29.62	3.0140	0.1891	33.6	43.45	
8.	**32.02**	**2.7933**	**0.2285**	**100.0**	**36.17**	**36.2 nm**
9.	41.92	2.1536	0.3673	20.6	23.16	

10.	42.04	2.1478	0.0255	20.6	334.11	
11.	42.85	2.1090	0.1165	15.7	73.25	
12.	43.42	2.0826	0.2493	16.3	34.30	
13.	45.73	1.9826	0.0314	22.1	274.19	
14.	45.79	1.9802	0.2603	22.9	33.13	
15.	56.74	1.6213	0.2413	15.9	37.42	

Band gap calculation:

UV-Vis absorption spectroscopy characterized the optical properties of $MnNiBa_2O_4$ nanoparticles (Figure 5). The absorption coefficient (α) was calculated as α = 2.303A/t, where A is absorbance and t is path length. Bandgap energy (3.25 eV) was determined by extrapolating the linear region of the $(\alpha h\nu)^2$ vs. hν Tauc plot to the x-axis (Figure 6), with a peak absorbance at 464 nm. This bandgap enhances charge separation and e^-/h^+ lifetimes, boosting photocatalytic pollutant mineralization [21-24]

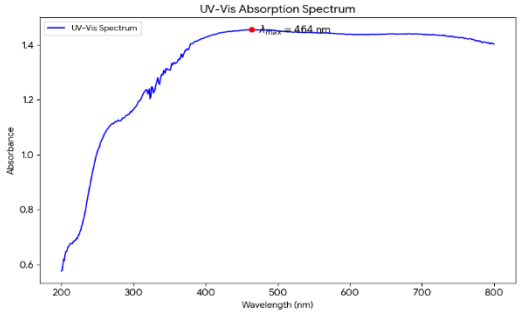

Figure 5. UV-VIS spectra peak absorption of $MnNiBa_2O_4$ photocatalyst

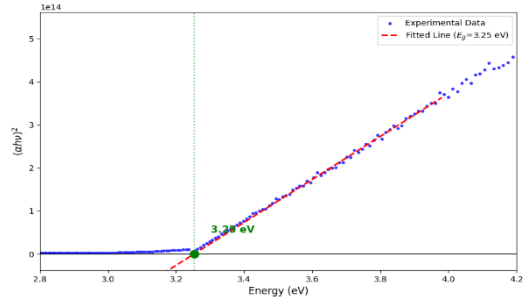

Figure 6. UV-VIS spectra for bandgap of MnNiBa2O4 photocatalyst

Photoluminescence (PL) Spectroscopy Analysis:

The electronic structure and optical properties of the $MnNiBa_2O_4$ mixed metal oxide photocatalyst were probed using photoluminescence (PL) spectroscopy (excitation at 290 nm), building on UV-Vis absorption data. The bandgap was measured at 3.25eV (≈382.7 nm), with a key absorption peak at 463.93 by Uv-vis absorption data. The PL spectrum (Figure 7) revealed distinct peaks revealing charge dynamics, including near-band-edge (NBE) emission at 427.5 nm (2.90 eV) [25][26].The shift from the 3.24 eV bandgap to the NBE peak stems from photoexcited electron relaxation into shallow trap/tail states prior to recombination is a frequent feature in Ba^{2+}-containing complex oxides [26] [27]. A prominent emission at 469.7 nm closely matches the 463.93 nm absorption, linked to crystal field d-d transitions of Mn^{2+} and Ni^{2+} in the Ba_2O_4 matrix, signalling strong visible-light harvesting and stable transitions [28]. Peaks at 349.6 nm and 445.1 nm signal intrinsic defects and oxygen vacancies, which trap carriers to prolong lifetimes and promote catalysis. This bandgap-PL interplay affirms $MnNiBa_2O_4$'s semiconducting integrity and potential for photocatalysis and remediation [29].

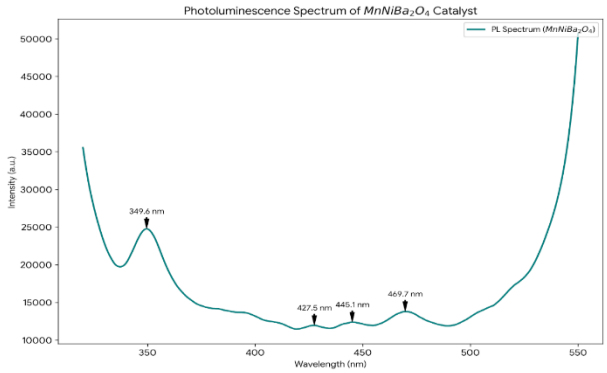

Figure 7. Photoluminescence Studies and Defect Analysis of $MnNiBa_2O_4$ photocatalyst

Photocatalytic activity of $MnNiBa_2O_4$ photocatalyst:

For kinetic study, solutions of toluidine blue was placed in a borosil beaker, pH was measured, photocatalyst was added, and exposed to light; optical density was recorded over time. Figure 8 displayed a linear plot of (1 + log O.D.) versus time. Pseudo-first-order kinetics formula best fit the degradation data among tested models (pseudo-first/second-order Types 1-5). Optimized toluidine blue dye degradation conditions obtained were pH 8.5, 0.14 g catalyst, 6.5×10^{-4} M dye concentration, 1640 mW/cm² light intensity.

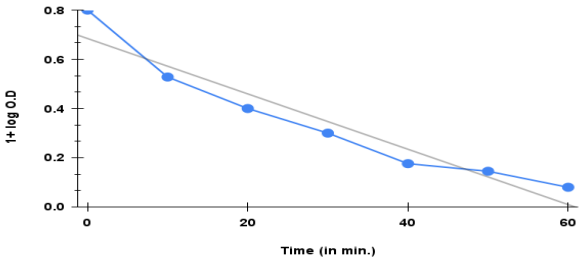

Figure 8: Photocatalytic activity of $MnNiBa_2O_4$ photocatalyst for degradation of toluidine blue Typical run

Effect of photocatalyst doses:

The impact of the photocatalyst dosage on the degradation process was meticulously investigated by varying its weight, while ensuring all other variables remained constant. Figure 9 vividly portrays the outcomes of this exploration. Interestingly, the highest degradation rate was observed for toluidine blue at a photocatalyst dose of 0.14g. This can be attributed to the increased surface area available for absorbing light radiation, thus generating a greater number of electron-hole pairs. Such an outcome is linked to the fact that a higher dosage of the photocatalyst leads to a larger surface area of particles exposed to light. However, upon further increasing the photocatalyst dose, an intriguing observation emerged: the reaction rate began to decline. This phenomenon is attributed to the recombination of electrons and holes, which occurs due to their enhanced quantity at higher photocatalyst doses.

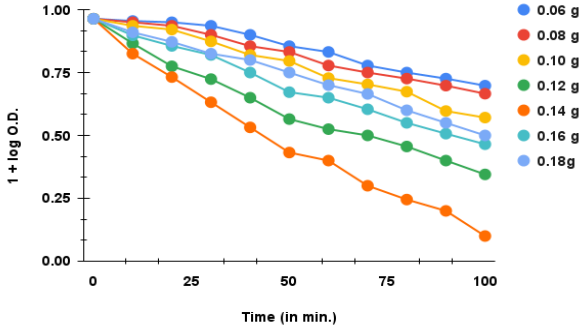

Figure 9: Photodegradation of toluidine blue by $MnNiBa_2O_4$ photocatalyst at different photocatalyst dosages (g)

Effect of dye concentration:

The study was conducted within the various range of dye concentration, with all other variables held constant. The resulting data for toluidine blue is illustrated in figure 10. Observations indicate that the reaction rate increases with an increase in the concentration of dye. This is because more dye molecules are available to absorb photons from light, becoming excited in the process. However, after reaching a maximum value (at 6.5 × 10-5 M), further increases in dye concentration leads to a decrease in the rate of degradation. This decline occurs because beyond a certain concentration, additional dye darkens the color of the reaction mixture and begins to act as a filter to the incident light.

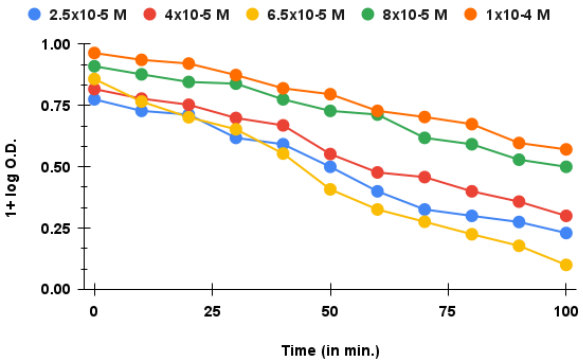

Figure 10: Photodegradation of toluidine blue by $MnNiBa_2O_4$ photocatalyst at different concentration of dyes

Effect of intensity of light:

The experiment entailed adjusting the light intensity within the range of 1320 to 1760 mW/cm², with corresponding data presented graphically in figure 11. All other experimental variables were kept constant throughout. It was noted that the rate of photocatalytic degradation increased in tandem with the rise in light intensity. This phenomenon can be attributed to the greater number of photons striking per unit area over time as light intensity escalates. Consequently, there is an increase in the presence of excited dye molecules and electron-hole pairs at the photocatalyst's surface. The peak degradation rates for toluidine blue was observed at a light intensity of 1640 mW/cm² after which they declined. This decrease can be attributed to the elevated probability of recombination of photogenerated electron-hole pairs at higher light intensities. Such recombination processes diminish the pool of reactive species available for dye degradation, thereby reducing overall efficiency.

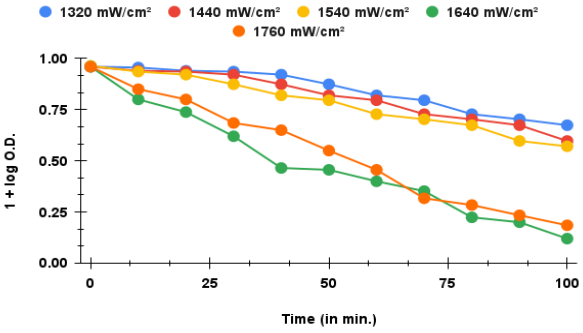

Figure 11: Photodegradation of toluidine blue by $MnNiBa_2O_4$ photocatalyst at different intensity of light

Effect of pH:

The breakdown speed of the dye changes significantly depending on the pH level of the solution because dye is quite sensitive to pH variations. Some dyes even alter their color when the pH changes. To understand this better, we systematically adjusted the pH of the solution while keeping all other factors constant. Interestingly, we noticed that the initial optical density of the solution changed as the pH varied, as shown in detailed graphs. Our study focused on the pH range of 3 to 10 with the results depicted in figures 12. This thorough analysis

reveals how crucial pH is in influencing the dye degradation process. We observed that the rate of photocatalytic degradation increased as the pH was raised for toluidine blue. The peak degradation points for toluidine blue was observed at pH 8.5. The explanation incorporates the participation of hydroxyl free radicals at higher pH where hole generated at photocatalyst surface abstracts electrons from water or hydroxyl anion to generate hydroxyl free radicals . These free radicals attack the weaker bond sites of dye molecules altering their conjugation, causing their degradation and breaking them in to smaller harmless fragments.

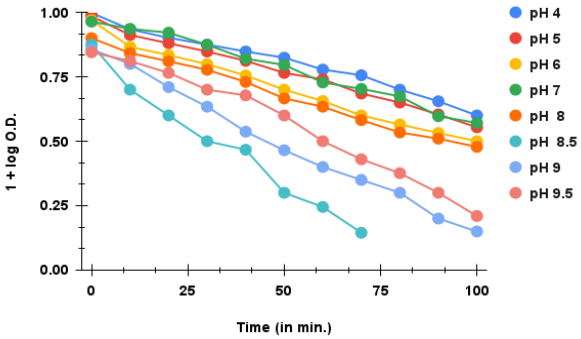

Figure 12: Photodegradation of toluidine blue by $MnNiBa_2O_4$ photocatalyst at different pH

Ascertaining the reactive species

To elucidate the mechanistic pathways and identify the primary reactive species responsible for the photocatalytic degradation of Toluidine Blue (TB), Eosin Yellow (EY), and Reactive Red 35 (RR-35), systematic radical trapping experiments were conducted. Specific scavengers were introduced to the reaction medium to selectively quench potential active species: Ethylenediaminetetraacetic acid (EDTA) and Potassium Iodide (KI) were employed as scavengers for photogenerated holes (h^+), Isopropanol (IPA) for hydroxyl radicals, and p-Benzoquinone (BQ) for superoxide radicals. In a typical procedure, 5% concentrations of these inhibitors were added to the respective dye solutions prior to the addition of the catalyst and subsequent irradiation [30]. The results is depicted in Figure 13, reveal a significant suppression of degradation efficiency in the presence of specific scavengers. Notably, the degradation of Toluidine Blue was profoundly inhibited by the addition of EDTA. This substantial reduction confirms that photogenerated holes (h^+) is the dominant oxidative species driving the degradation dyes.

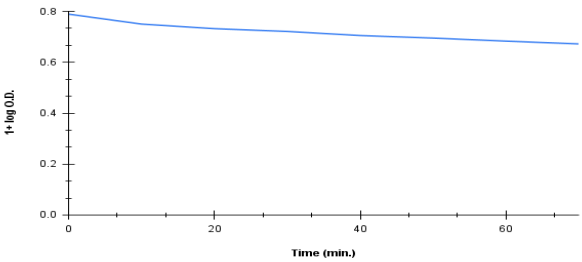

(a)

Figure 13: Photodegradation of toluidine blue by $MnNiBa_2O_4$ photocatalyst with scavenger

Mechanism

A generalized mechanism for all examined dyes is proposed here by:

(1) 1Dye0 (TB, EY and RR) →1Dye1 (Singlet excited state)

(2) 1Dye1 (TB, EY and RR) →1Dye3 (Triplet excited state)

(3) $MnNiBa_2O_4$ + Light photon (hv) → $MnNiBa_2O_4$ [e^- (CB) + h^+ (VB)]

(4) $e^- + O_2 \rightarrow O_2^{\bullet -}$

(5) $h^+ + H_2O \rightarrow OH^\bullet + H^+$

(6) $h^+ + OH^- \rightarrow OH^\bullet$

(7) Dyes + $O_2^{\bullet -} \rightarrow CO_2 + H_2O + N_2 + NO_2$ etc.

(8) Dyes + $OH^\bullet \rightarrow CO_2 + H_2O + N_2 + NO_2$ etc.

The last two steps for each individual dye (TB, EY and RR) depending on which radical ($O_2^{\bullet -}$ or •OH) scavenger studies identify as the dominant oxidizing species.

Recycling of the $MnNiBa_2O_4$ photocatalyst

The recovered photocatalyst was recycled i.e. washed and calcined again. This was then used for degradation of all dyes and it was observed that its efficiency remained unaltered even after its repeated use for next four cycles. This property makes it more valuable to be used as potential photocatalyst in environmental remediation.

CONCLUSION

This study successfully demonstrates the synthesis of $MnNiBa_2O_4$ nanoparticles via the co-precipitation method, achieving a high yield of 90.72%. Comprehensive characterization using XRD, FE-SEM, and XPS confirmed a stable structure with an average crystallite size of ~36 nm and an optical band gap of 3.25 eV. The synthesized nanoparticles exhibited excellent photocatalytic potential for the degradation of organic pollutants toluidine Blue. Detailed optimization experiments revealed distinct pH preferences for efficient degradation: alkaline conditions were found to be optimal. Furthermore, the degradation kinetics were shown to be sensitive to light intensity and initial dye concentration. Overall, the $MnNiBa_2O_4$ photocatalyst proves to be an effective and versatile candidate for wastewater treatment and environmental purification applications.

REFERENCES

1. Khan S, Noor T, Iqbal N, Yaqoob L. Photocatalytic dye degradation from textile wastewater: a review. ACS Omega. 2024;9(20):21751-21767.

2. Kumari H, Sonia, Suman, Ranga R, Chahal S, Devi S, et al. A review on photocatalysis used for wastewater treatment: dye degradation. Water Air Soil Pollution. 2023;234(6):349.

3. Hamza M, Altaf AA, Kausar S, Murtaza S, Shahpal A, Hamayun M, et al. Mesoporous Cu-doped manganese oxide nano straws for photocatalytic degradation of hazardous alizarin red dye. ACS Omega. 2023;8(39):35956-35963.

4. Xu Z, Zada N, Habib F, Ullah H, Hussain K, Ullah N, et al. Enhanced photocatalytic degradation of malachite green dye using silver–manganese oxide

nanoparticles. Molecules. 2023;28(17):6241.
5. Li H, Fu B, Huang H, Wu S, Ge J, Zhang J, et al. Catalytic degradation of organic pollutants by manganese oxides: a comprehensive review. Environmental Pollutants and Bioavailability. 2022;34(1):395-406.
6. Adekunle AS, Oyekunle JA, Durodola SS, Durosinmi LM, Doherty WO, Olayiwola MO, et al. Photocatalytic Degradation of dyes in wastewater using solar enhanced nickel oxide (NiO) nanocatalysts prepared by chemical methods. Journal of Fluorescence. 2025;35(1):257-265.
7. Siddique K, Azeem F, Attia KA, Hussain S, Shahid M, Fiaz S, et al. Comparative efficacy of biologically and chemically synthesized nickel oxide nanoparticles for catalytic degradation of dyes and wastewater treatment. Scientific Reports. 2025;15(1):34666.
8. Nandiyanto ABD, Ragadhita R, Anggiat LS. Synthesis of barium oxide nanoparticles: Optical properties and application in degradation indigotine dye. Moroccan Journal of Chemistry. 2024;12(2):627-642.
9. Basavanagoudra H, Jangannanavar VD, Patil MK, Inamdar SR, Goudar KM. Barium oxide nanorods: Catalyst concentration and surface defects' role in degrading methylene blue organic pollutant. Chemical Physics Impact. 2024;8:100578.
10. Verhoeven JT, Van Doveren H. XPS studies on Ba, BaO and the oxidation of Ba. Applications of Surface Science. 1980;5(4):361-373.
11. Karslıoğlu O, Trotochaud L, Zegkinoglou I, Bluhm H. X-ray spectroscopic characterization of BaO, $Ba(OH)_2$, $BaCO_3$, and $Ba(NO_3)_2$. Journal of Electron Spectroscopy and Related Phenomena. 2018;225:55-61.
12. Di Castro V, Polzonetti G. XPS study of MnO oxidation. Journal of Electron Spectroscopy and Related Phenomena. 1989;48(1):117-123.
13. Di Castro V, Ciampi S. XPS study of the growth and reactivity of Fe/MnO thin films. Surface Science. 1995;331:294-299.
14. Biesinger MC, Payne BP, Grosvenor AP, Lau LW, Gerson AR, Smart RSC. Resolving surface chemical states in XPS analysis of first row transition metals, oxides and hydroxides: Cr, Mn, Fe, Co and Ni. Applied Surface Science. 2011;257(7):2717-2730.
15. Bagus PS, Nelin CJ, Brundle CR, Crist BV, Ilton ES, Lahiri N, Rosso KM. Main and satellite features in the Ni 2p XPS of NiO. Inorganic Chemistry. 2022;61(45):18077-18094.
16. Cussen EJ, Battle PD. Crystal and magnetic structures of 2H $BaMnO_3$. Chemistry of Materials. 2000;12(3):831-838.
17. Pena MA, Fierro JLG. Chemical structures and performance of perovskite oxides. Chemical Reviews. 2001;101(7):1981-2018.
18. Monshi A, Foroughi MR, Monshi MR. Modified Scherrer equation to estimate more accurately nano-crystallite size using XRD. World Journal of Nano Science and Engineering. 2012;2(3):154-160.
19. Osterloh FE. Inorganic materials as catalysts for photochemical splitting of water. Chemistry of Materials. 2008;20(1):35-54.
20. Ungár T. Microstructural parameters from X-ray diffraction peak broadening. Scripta Materialia. 2004;51(8):777-781.
21. Amjad M, Bibi I, Majid F, Jilani K, Sultan M, Raza Q, Iqbal M. $NiO/MnFe_2O_4$ nanocomposite photoluminescence, structural, morphological, magnetic, and optical properties: photocatalytic removal of cresol red under visible light irradiation. ACS Omega. 2024;9(19):20876-20890.
22. Suram SK, Zhou L, Shinde A, Yan Q, Yu J, Umehara M, Gregoire JM. Alkaline-stable nickel manganese oxides with ideal band gap for solar fuel photoanodes. Chemical Communications. 2018;54(36):4625-4628.
23. Islam R, Abdur R, Alam MA, Munna N, Ahmed AN, Hossain M, Jamal MS. Modulating Mn-doped NiO nanoparticles: structural, optical, and electrical property tailoring for enhanced hole transport layers. Nanoscale Advances. 2025;7(1):133-143.
24. Parimon N, Mamat MH, Banu IS, Vasimalai N, Ahmad MK, Suriani AB, Rusop M. Annealing temperature dependency of structural, optical and electrical characteristics of manganese-doped nickel oxide nanosheet array films for humidity sensing applications. Nanomaterials and Nanotechnology. 2021;11:1847980420982788.
25. Wang J, Xu Z, Xu Y, Liu S, Qiu J, Wang Z, et al. Mn single atoms for one-electron photoozonation of aqueous organics. Applied Catalysis B: Environmental. 2024;349:123900.
26. Rajendran S, Vijayaraghavan R. Oxygen vacancies mediated enhanced photocatalytic activity of band gap engineered BaSn1-xCuxO3 towards methylene blue degradation under visible and sunlight. RSC Advances. 2025;15(30):24802-24814.
27. Manju, Jain M, Madas S, Vashishtha P, Rajput P, Gupta G, et al. Oxygen vacancies induced photoluminescence in SrZnO2 nanophosphors probed by theoretical and experimental analysis. Scientific Reports. 2020;10(1):17364.
28. Lakshminarayana G, Buddhudu S. Spectral analysis of Mn^{2+}, Co^{2+} and Ni^{2+}: B_2O_3–ZnO–PbO glasses. Spectrochimica Acta Part A: Molecular and Biomolecular Spectroscopy. 2006;63(2):295-304.
29. Thesing A, Loguercio LF, Vaz MO, Khattak MR, Franciosi G, Lieberknecht G, et al. Surface Oxygen Vacancies in Hierarchical Metal Oxide Nanostructures: Optoelectronic Tuning in Photocatalysis. Journal of Physical Chemistry C. 2024;128(50):21479-21487.
30. Microchemical Journal. A critical view about use of scavengers for reactive species in heterogeneous photocatalysis. Microchemical Journal. 2020;157:105013.